Brain Stimulation 14 (2021) 488–497

Contents lists available at ScienceDirect

Brain Stimulation

journal homepage: http://www.journals.elsevier.com/brain-stimulation

Safety evaluation of a new setup for transcranial electric stimulation during magnetic resonance imaging

Fróði Gregersen [a, b, c, h], Cihan Göksu [b, d], Gregor Schaefers [e, f], Rong Xue [g, h, i], Axel Thielscher [a, b, 1], Lars G. Hanson [a, b, *, 1]

[a] Section for Magnetic Resonance, DTU Health Tech, Technical University of Denmark, Kgs Lyngby, Denmark
[b] Danish Research Centre for Magnetic Resonance, Centre for Functional and Diagnostic Imaging and Research, Copenhagen University Hospital Amager and Hvidovre, Hvidovre, Denmark
[c] Sino-Danish Center for Education and Research, Aarhus, Denmark
[d] High-Field Magnetic Resonance Center, Max-Planck-Institute for Biological Cybernetics, Tübingen, Germany
[e] MRI-STaR-Magnetic Resonance Institute for Safety, Technology and Research GmbH, Gelsenkirchen, Germany
[f] MR:comp GmbH, MR Safety Testing Laboratory, Gelsenkirchen, Germany
[g] State Key Laboratory of Brain and Cognitive Science, Beijing MRI Center for Brain Research, Institute of Biophysics, Chinese Academy of Sciences, Beijing, 100101, China
[h] University of Chinese Academic of Sciences, Beijing, 100049, China
[i] Beijing Institute for Brain Disorders, Beijing, 100053, China

ARTICLE INFO

Article history:
Received 20 August 2020
Received in revised form
7 January 2021
Accepted 26 February 2021
Available online 9 March 2021

Keywords:
MR current Density imaging
MR electrical Impedance tomography
Transcranial electric stimulation
Safety

ABSTRACT

Background: Transcranial electric stimulation during MR imaging can introduce safety issues due to coupling of the RF field with the stimulation electrodes and leads.
Objective: To optimize the stimulation setup for MR current density imaging (MRCDI) and increase maximum stimulation current, a new low-conductivity ($\sigma = 29.4$ S/m) lead wire is designed and tested.
Method: The antenna effect was simulated to investigate the effect of lead conductivity. Subsequently, specific absorption rate (SAR) simulations for realistic lead configurations with low-conductivity leads and two electrode types were performed at 128 MHz and 298 MHz being the Larmor frequencies of protons at 3T and 7T. Temperature measurements were performed during MRI using high power deposition sequences to ensure that the electrodes comply with MRI temperature regulations.
Results: The antenna effect was found for copper leads at ¼ RF wavelength and could be reliably eliminated using low-conductivity leads. Realistic lead configurations increased the head SAR and the local head SAR at the electrodes only minimally. The highest temperatures were measured on the rings of center-surround electrodes, while circular electrodes showed little heating. No temperature increase above the safety limit of 39 °C was observed.
Conclusion: Coupling to the RF field can be reliably prevented by low-conductivity leads, enabling cable paths optimal for MRCDI. Compared to commercial copper leads with safety resistors, the low-conductivity leads had lower total impedance, enabling the application of higher currents without changing stimulator design. Attention must be paid to electrode pads.

Introduction

Roughly two decades ago, Nitsche and Paulus showed that human motor cortex excitability could be non-invasively modulated by weak electric currents applied through the intact skull by surface electrodes [1]. Since then, the use of transcranial electric stimulation (TES) techniques in neuroscience applications has grown tremendously. There is also increasing interest to apply TES inside magnetic resonance imaging (MRI) scanners. This is

* Corresponding author. Danish Research Centre for Magnetic Resonance, Centre for Functional and Diagnostic Imaging and Research, Copenhagen University Hospital Hvidovre, Section 714, Kettegaard Allé 30, 2650, Hvidovre, Denmark.
E-mail address: larsh@drcmr.dk (L.G. Hanson).
[1] These authors contributed equally to this work.

https://doi.org/10.1016/j.brs.2021.02.019

motivated by the wish to use functional MRI (fMRI) for characterizing the physiological stimulation effects. More recently, MRI is also applied to shed light on the physical current flow inside the brain. Simulation of the current flow using forward models of the head anatomy [2,3] is feasible, but the accuracies and reliabilities of the results are challenged by a number of factors. For example, the ohmic conductivities of the head tissues at low frequencies are quite uncertain, highlighting the need to validate the simulated fields [4].

MR current density imaging (MRCDI) [5] and MR electrical impedance tomography (MREIT) [6] are two emerging modalities that can indirectly measure the current flow in the brain and the conductivity of the tissue, respectively. These techniques have the potential to improve the accuracy of electric field simulations for TES, as well as for source localization in electro- and magnetoencephalography (EEG and MEG) [7], and can aid in the characterization of pathological tissue [8]. Similar to TES, MRCDI and MREIT use weak currents applied via surface electrodes. The current-induced changes of the static magnetic field are measured and used to determine the current flow or tissue conductivities at low frequency.

The current flow inside the brain changes the magnetic field only slightly, resulting in a low signal-to-noise ratio (SNR) of the measurements and making them prone to artifacts. The effect of the stray fields from the cable currents has previously been studied [9]. Unless the leads are aligned fully parallel to the main magnetic field, the induced stray fields will strongly influence the current-induced magnetic field changes measured in the brain, and therefore the current density and conductivity reconstruction. This can be corrected for by tracking the cables in MR images and using the Biot-Savart law to subtract induced stray fields [10]. Although the correction method significantly improves the current density reconstruction results, it would be preferable to orient the leads parallel to the main magnetic field to reduce residual errors and increase the robustness of the measurement approach.

For TES, MRCDI and MREIT, the currents are applied through lead wires connected to the subject's scalp via surface electrodes. Extra safety measures have to be taken when conductive materials are used in an MR scanner, especially when in contact with tissue. Many incidences of patient burns caused by coupling between the RF field and lead wires have been reported [11]. However, no burn incidents have been reported for TES-MRI. Heating of leads can be caused by direct electromagnetic induction in wire loops [12] and highly conductive loops must be avoided during MRI. Another important origin of heating is the antenna effect that occurs when wires or other conductors of appropriate length act as "receive antennas" for the RF field. For increasing field strengths, the antenna effect becomes an increasing problem due to the shorter wavelength of the RF field. Half a wavelength is typically found to be the critical length for heating [13,14], but it has been shown experimentally that the length of the lead required to observe the effect also depends on the boundary conditions on each end of the lead [15]. For high impedance at one end (open or connected to a safety resistor or high impedance amplifier) and relatively low impedance at the other end (connected to tissue) ¼ RF wavelength can be critical as well. Therefore, the design of lead wires that reliably prevent the occurrence of electromagnetic induction and antenna effects despite varying boundary conditions is important, but challenging.

Conventional TES devices use highly conductive leads (usually copper) between the stimulator and surface electrodes. For the TES device that is most commonly used in combination with MRI (DC-STIMULATOR MR, neuroCare Group GmbH, München, Germany), most of the cable is realized as twisted pair cable and 5 kΩ safety resistors are added to each of the two leads to limit the length of highly conductive material near the scanned subject (Fig. 1a). This design improves safety but prevents an optimal cable orientation for MRCDI and MREIT experiments. Because the device supplies a maximal output voltage of 30 V, the safety resistors also limit the maximum possible stimulation current to around 2 mA. Most TES studies so far have used currents up to 2 mA, but there is recent interest to explore higher current strength of up to 4 mA to increase efficacy [16–20]. The safety resistors limit the use of TES-fMRI studies to characterize the physiological effect of higher TES currents.

The aim of this work is to redesign the leads for combined MR and current injection experiments to remove the above restrictions. Specifically, the goal was to develop leads that would allow long straight wire paths parallel to the static magnetic fields and support stimulation currents up to 4 mA with the existing stimulator while not compromising safety. Instead of using highly conductive materials and local safety resistors, we propose to use a distributed resistance by having leads with much lower conductivity, while also having an overall lower total impedance. Carbon fiber leads are routinely used for EEG-MRI and are reported to decrease specific absorption rate (SAR) compared to copper leads [21]. Here, we extend this approach to TES and further minimize the risk for the occurrence of antenna effects by using an even less conductive silicone rubber material (σ = 29.4 S/m) for the lead wires. Numerical methods have previously been used to estimate SAR for combined EEG-MRI studies [21–23], as well as for TES-MRI experiments [24,25].

In this study, we use both numerical simulations to estimate SAR as well as experimental temperature measurement. We first simulate a worst-case antenna effect at 298 MHz to investigate the relationship between the antenna effect and conductivity. Secondly, we simulate two electrode types with various lead configurations to ensure safety at both 128 MHz and 298 MHz, corresponding to the proton Larmor frequencies at 3T and 7T magnetic field strength. Lastly, temperature measurements are performed on the electrodes and leads made in-house during in vivo MRI at both field strengths.

Methods

Electrode and lead design

We constructed two commonly used TES electrode types in-house: 1) The circular electrode commonly used for non-focal stimulation in TES or for MRCDI and MREIT (Fig. 1b) and 2) the center-surround electrode used for focal stimulation in TES experiments [26] (Fig. 1c). Both types are 3 mm thick. The circular electrodes are 5 cm in diameter. The center-surround electrodes have an outer ring with an inner and outer diameter of 10 cm and 8 cm, respectively. The diameter of the center electrode is 3 cm. For all electrodes, a 90 cm silicone rubber strip with a cross-sectional area of 10 mm^2 was cut out and used as the lead wire. Both electrodes and leads are made from silicone rubber (ELASTOSIL® R 570/60 RUSS, Wacker, Munich, Germany). The resistance of each of the lead wires is 2 kΩ ± 200 Ω. To ensure proper electrical connection and mechanical strength, the rubber leads are sewed on to the electrodes. The other ends of the leads are connected to copper leads with cable crimps. Medical grade touch-proof safety connectors are connected to the copper leads (MS1525-B, Stäubli, Pfäffikon, Switzerland). A glass-fiber braided sleeving (GSS6, HellermannTyton, Crawley, Germany) is used for thermal and electrical insulation. The glass-fiber sleeving is also sewed on to the electrode and connected to the copper wire to relieve the silicone rubber lead of any strain. Ten20 conductive EEG paste (D.O. Weaver and Co.,

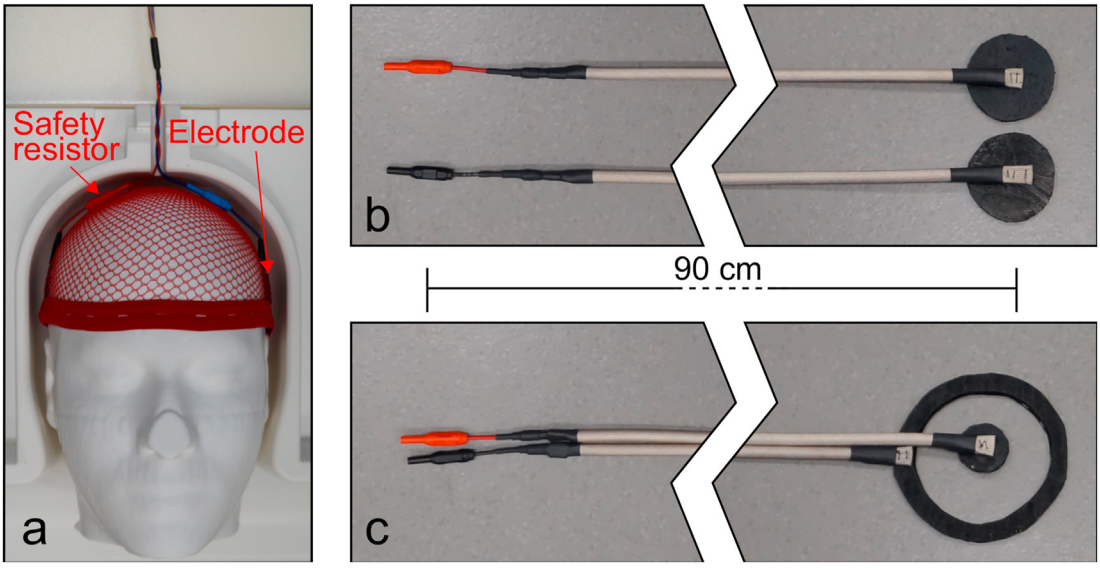

Fig. 1. a) Commercially available TES-MRI setup (DC-STIMULATOR MR, neuroCare Group GmbH, München, Germany) with copper lead wires and 5 kΩ safety resistors. Leading the wires in the superior direction through the opening in the coil and using twisted pair cables restricts the lead configuration and causes stray fields compromising MRCDI experiments. b) and c) show the proposed circular and center-surround electrode and the lead design, respectively. Low-conductivity silicone rubber ($\sigma = 29.4$ S/m) is used for electrodes and leads (black) thermally and electrically shielded with a glass fiber sleeving (gray). Medical grade touch-proof MC connectors are used to connect the electrodes to copper lead wires 90 cm away from the subject's head.

Aurora, CO, USA) is used between the electrodes and abraded skin to ensure proper connection.

Simulations

Finite-difference time-domain (FDTD) simulations were performed in Sim4Life (ZMT, Zurich, Switzerland) to obtain specific absorption rate (SAR) results. Simulations were performed with 128 MHz and 298 MHz harmonic excitations. All simulations ran until convergence at −30 dB, tested for steady-state on the lumped elements and sources on the RF coils.

Phantom

The heterogeneous male body model Duke from the IT'IS foundation was used in the simulations [27]. The head was positioned at the centers of the birdcage coils in all simulations. 2 mm isotropic resolution was used for Duke's head and shoulders and 4 mm for the torso. The rest of the body was segmented according to the automatic gridding produced by Sim4Life. This was done to reduce simulation time while still allowing sufficient current flow to obtain accurate simulation results [28].

RF coils

For 128 MHz simulations, a generic body coil was used (Fig. 3). Although the proton Larmor frequency of the scanner used in the experiments is 123 MHz the small difference in frequency will have minimal influence on the results. The 298 MHz coil (Fig. 2a) is a model of a transmit head coil [29] (7T volume T/R, Nova Medical, Wilmington, MA). Both coils are 16 rung high-pass birdcage coils. The dimensions are given in Table 1. The coils have two input ports on the superior end-ring 90° apart shifted 45° relative to the body model. The coils were iteratively tuned to the respective frequencies loaded with Duke with the head placed in the centers of the coils. The coils were driven in quadrature mode with equal input power on both ports. For coil model validation, see S2 in supplementary materials.

SAR evaluation

SAR is a measure of the RF power absorbed by the tissue and is given by

$$SAR = \frac{\sigma}{2\rho}\left|\vec{E}\right|^2, \tag{1}$$

where σ is the tissue conductivity, ρ is the density of tissue end $\left|\vec{E}\right|$ is the peak electric field inside the tissue.

According to international guidelines IEC 60601-2-33 [30], SAR is limited during MRI to avoid excessive heating of a subject due to absorbed RF power. The two relevant limitations for head MRI are head SAR (SAR averaged over the mass of the head) and local head SAR given as the peak spatial average SAR over 1 g or 10 g of tissue. To evaluate the influence that the electrodes and leads have on SAR, we compare head SAR and 1 g local head SAR for a reference simulation to simulations that include electrodes. The head SAR and 1 g local head SAR ratios are expressed as

$$R_m = \frac{HeadSAR}{HeadSAR_{ref}},\ R_{1g} = \frac{SAR_{1g}}{SAR_{1g_{ref}}}. \tag{2}$$

SAR is compared for 1 W radiated power as well as for a calibrated B_1 field. The input power P for each simulation is scaled such that the average amplitude of B_1 in the center slice of the coil is the same for all simulations. This is done the following way:

$$P = P_{ref}\left(\frac{B_{1,ref}}{B_1}\right)^2. \tag{3}$$

P_{ref} is the input power for the reference simulation, set to 1 W, $B_{1,ref}$ is the average B_1 amplitude for the center slice of the reference simulations, and B_1 is the average B_1 amplitude for the corresponding simulation before normalization.

The electrodes, leads, and gel are excluded when R_m and R_{1g} are calculated to include only tissue SAR when averaging is performed. By excluding the electrodes from R_m and R_{1g} calculations, these

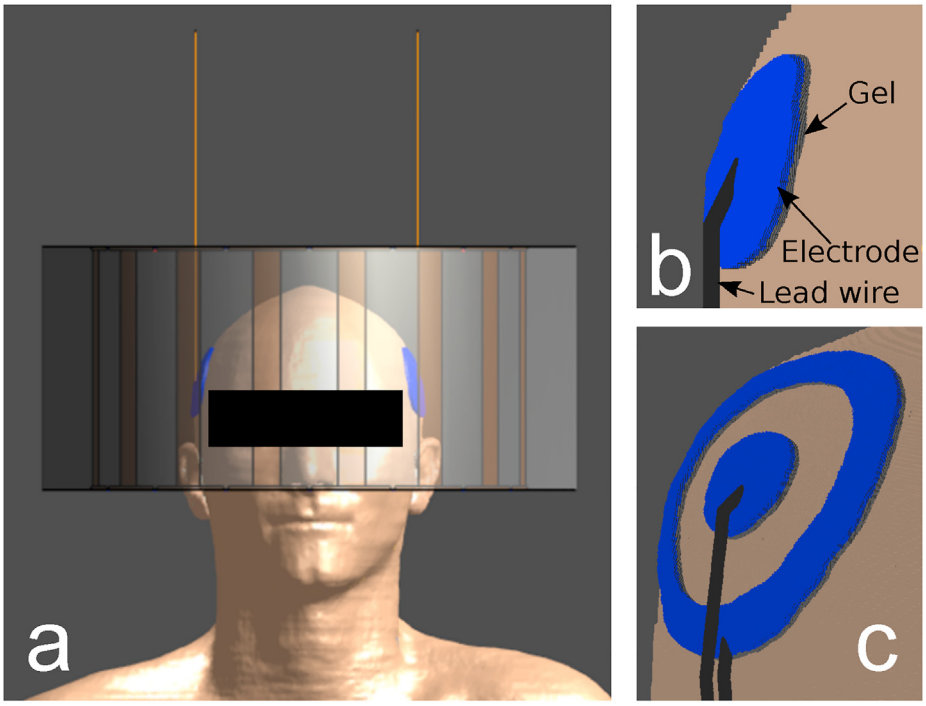

Fig. 2. a) Coil model for 298 MHz simulations with electrodes and straight leads to investigate the relationship between the antenna effect and conductivity. Circular (b) and center-surround electrode (c) montages including leads, electrodes and gel connected to the scalp, modeled with an isotropic grid with 0.5 mm resolution.

values only express the changes in SAR on the tissue caused by adding electrodes and not the power loss in the electrodes and the gel. Temperature measurements are used to ensure that the heating caused by the power loss in the electrodes and gel is within regulation limits [30].

Antenna effect simulations

To examine the relationship between the antenna effect and the conductivity of the lead wires, a worst-case simulation was performed with the lead wires parallel to the z-direction with one end connected to the circular electrodes and one end in free space as seen in Fig. 2a. This simulation was only performed at 298 MHz as the antenna effect becomes an increasing problem for higher frequencies. The simulations were performed with varying lead lengths from 0 to 100 cm with 10 cm increments including 25 cm and 75 cm as they are approximately ¼ and ¾ wavelength in air at the proton Larmor frequency 298 MHz. Two conductivities were used for all the incremental lengths of the lead wires, namely $5.8 \cdot 10^7$ S/m for copper and 29.4 S/m for silicone rubber with constant cross-sectional area. For 25 cm (the worst-case length), multiple conductivities were simulated with logarithmic increments from 10^2 S/m to 10^7 S/m. The average power dissipation on the electrodes is used as a measure of the severity of the antenna effect.

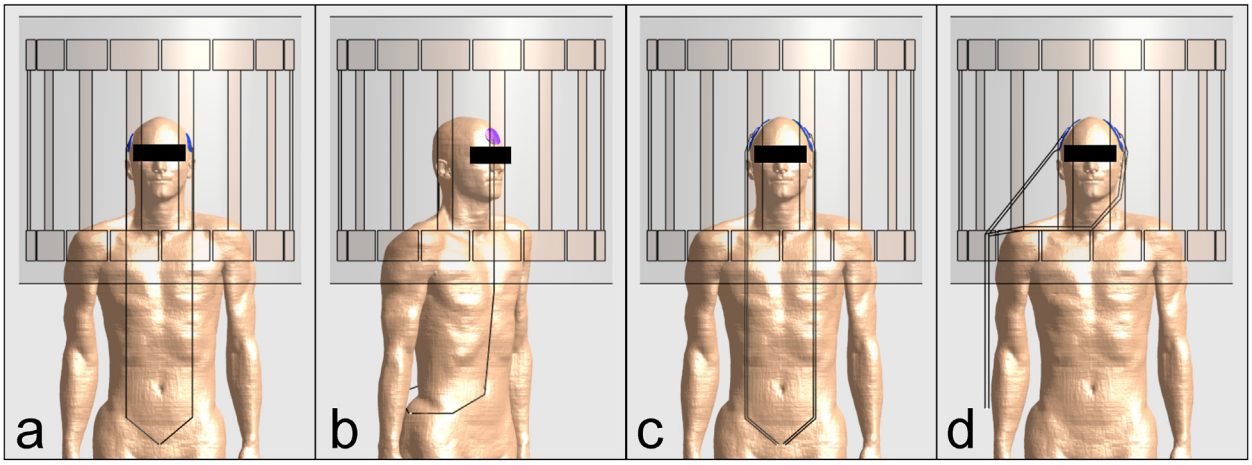

Fig. 3. Four lead configurations were simulated for both field strengths. Although only shown for the 128 MHz body coil here, the simulations were also performed for the 298 MHz head coil seen in Fig. 2a. Right-left (a) and anterior-posterior (b) montages for the circular electrodes were simulated with intended lead configurations as central as possible in the coil and with straight leads to reduce stray fields for MRCDI. For the center-surround electrodes, right-left montage with the intended lead configuration (c) was simulated as well as a worst case with leads closer to the coil (d), where the E-field is higher.

Table 1
Dimensions for the coil models used in the simulations.

	128 MHz (3T)	298 MHz (7T)
No. of Legs	16	16
Coil Radius	352 mm	155 mm
Leg Length	420 mm	168 mm
Leg Width	40 mm	20 mm
Endring Width	80 mm	2.5 mm
Shield Radius	371.5 mm	190 mm
Shield Length	700 mm	173 mm

Realistic lead configuration simulations

For the realistic lead configurations, simulations were performed for the center-surround and circular electrodes at 128 MHz and 298 MHz, respectively. Four lead configurations were simulated as seen in Fig. 3. A right-left and an anterior-posterior montage were simulated for the circular electrodes (Fig. 3a and b). The center-surround electrodes were only simulated for a right-left montage (Fig. 3c). The lead configurations in Fig. 3a–c show the intended use cases. In addition, the lead configuration in Fig. 3d was also simulated to ensure that misplacing the leads will not have critical consequences due to higher E-field close to the RF coil. All three electrode montages were also simulated without leads for both magnetic field strengths. The electrodes and gel are shown in Fig. 2b and c. The add-on subgrid feature using the Acceleware GPU solver (Acceleware, Calgary, Canada) in Sim4Life was used to obtain a fine resolution for electrode, gel and leads while keeping the same grid size in the rest of the simulation space. An isotropic grid size of 0.5 mm was used for electrodes, gel and leads. With this resolution, the smallest structure in any direction is minimum 4 times the grid size.

The conductivity σ and the relative permittivity ε_r for both the silicone rubber and the conductive gel, used between the electrodes and the skin, were measured with an ENA Series Network Analyzer E5071C and an open-ended probe 85070A (Agilent Technologies, Santa Clara, CA) at relevant frequencies to ensure more accurate simulations. For silicone rubber $\sigma = 29.4$ S/m and $\varepsilon_r = 6$ were used for both frequencies. For the Ten20 gel $\sigma = 0.86$ S/m and $\varepsilon_r = 36.61$ were used at 128 MHz and $\sigma = 0.95$ S/m and $\varepsilon_r = 32.55$ at 298 MHz.

The leads were terminated with an equivalent resistor representing the output impedance of the combined copper cable, filter, and stimulator (DC-STIMULATOR MR, neuroCare Group GmbH, München, Germany). The output impedances at the relevant simulation frequencies were found with a vector network analyzer (VNA). Since the leads are 90 cm long, the equivalent resistors are far outside the effective exposure volume of the coils as seen in Fig. 3.

Experimental setup

Experiments were performed on 3T (MAGNETOM Prisma; Siemens Healthcare, Erlangen, Germany) and 7T (Achieva; Philips Healthcare, Best, The Netherlands) whole-body MRI scanners. Two senior researchers involved in the project were scanned in the experiments. Informed consent was obtained from the participants prior to the MR scans. The touch-proof safety connectors on the electrode leads were connected via a Biopac MECMRI-1 cable to the Biopac MRIRFIF pi filter (BIOPAC Systems, Goleta, USA). The filter reduces noise from the outside and is located in a panel between the scanner room and the control room. For stimulation, a neurostimulator will be connected to the filter on the control room side. The neurostimulator was not used in the experiments as the output impedance of the copper cable and filter remained the same independent of the stimulator. For safety assessment of electrodes and leads, temperature measurements were performed in the 3T and 7T scanners. Image quality assessment and imaging of the leads for stray field correction in MRCDI was performed at 3T. See S1 in the supplementary material for further details and results.

Temperature measurements

For temperature measurements at 3T, the built-in birdcage body coil was used as the transmit coil while at 7T, a birdcage head coil was used for excitation (7T volume T/R, Nova Medical, Wilmington, MA). Fiber-optic probes (Opsens Solutions, Quebec City, Canada) were used to measure the temperature. Four probes were available. The probes were placed in the gel between the electrode and the scalp at various locations indicated in Table 3 and Fig. 6a and b. When a reference probe was used, it was taped to the top of the head of the subject and insulated with a pad to better imitate the scenario of the other probes.

A Rapid Acquisition with Relaxation Enhancement (RARE) sequence was used for both field strengths to obtain a high SAR for the temperature measurements. The sequence parameters were adjusted to obtain approximately 100% reported SAR by the scanner relative to the SAR limit. At 3T, the RARE sequence parameters were repetition time $T_R = 175$ ms, echo time $T_E = 100$ ms, refocusing tip angle $= 180°$, echo train length $= 15$, image matrix $512 \times 512 \times 27$ and resolution $0.43 \times 0.43 \times 5.2$ mm^3. And at 7T, $T_R = 3584$ ms, $T_E = 47.54$ ms, echo train length $= 9$, image matrix $768 \times 768 \times 33$, resolution $0.28 \times 0.28 \times 3$ mm^3 and a varying refocusing tip angle. A Pseudo Continuous Arterial Spin Labeling (pCASL) sequence ($T_R = 4100$ ms, $T_E = 18$ ms, excitation tip angle $= 90°$, image matrix $73 \times 73 \times 60$, resolution $3 \times 3 \times 4$ mm^3, tag duration/tag delay $= 1500/1800$ ms, tag pulse angle $= 24°$ and tag gradient strength $= 7$ mT/m) was also used at 3T, as it is a relatively high SAR sequence that will potentially be used for TES-MRI studies. About 50% SAR was reported for the pCASL sequence. The sequences ran for 20 min to achieve sufficient data to accurately model the temperature increase and find the steady-state temperature. The model used is

$$T(t) = T_{ss} - \Delta T \cdot e^{-\frac{t}{t_C}}, \quad (4)$$

where $T(t)$ is the temperature at time t, T_{ss} is the steady-state temperature, ΔT is the difference between the start and steady-state temperature, and t_C is the time constant of the exponential term.

Stray field comparison

An MRCDI experiment with 1 mA current injection was performed to illustrate the change of stray fields from the leads when the improved lead configuration is used. Lead configurations seen in Fig. 1a and our proposed use as seen in Fig. 3a were compared. See Göksu et al. [10] for further details on the used MRCDI method. The imaging of silicone rubber used for cable tracking is presented in supplementary material S1.

Results

Antenna effect

Simulations with varying copper lead lengths showed that the antenna effect occurs at odd multiples of ¼ RF wavelength with ¼ being worse than ¾ (Fig. 4a). The same simulations but with low-conductivity silicone rubber showed that the antenna effect is eliminated with this material (Fig. 4a). Further investigation of the relationship between the antenna effect and conductivity at the worst-case length (25 cm) is shown in Fig. 4b. Carbon fiber leads

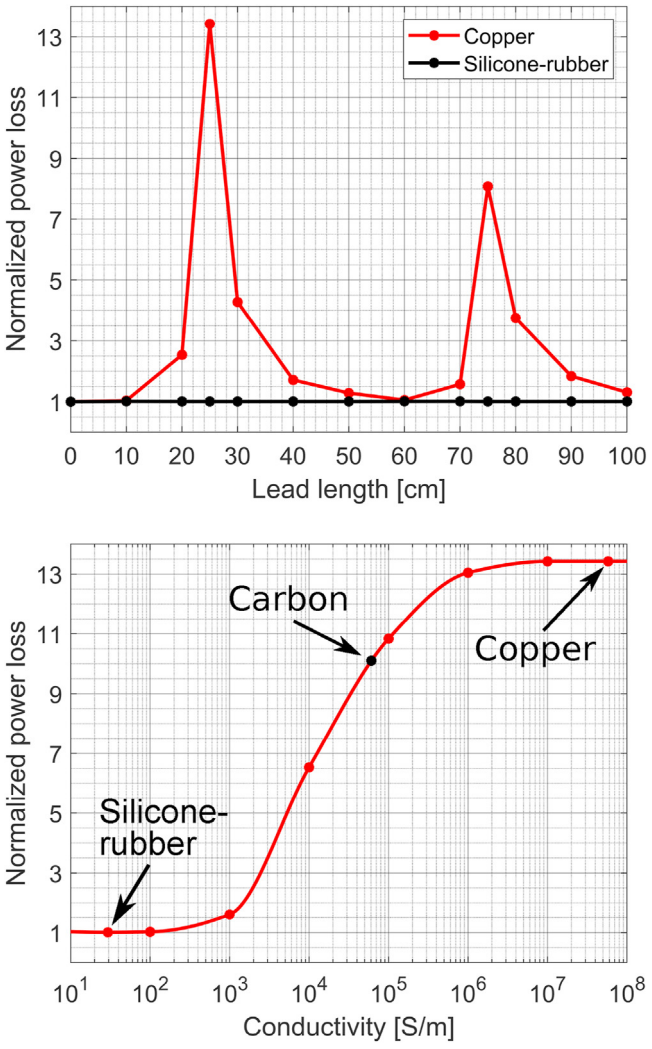

Fig. 4. a) Power loss on electrodes vs lead length for antenna effect simulations seen in Fig. 2a for copper and silicone rubber, respectively. b) Power loss on electrodes vs conductivity of 25 cm long leads shown to be the worst case. Power loss is normalized to average power loss on both electrodes without attached leads.

with a conductivity of $6.1 \cdot 10^4$ S/m [31] only reduces the severity of the antenna effect by about 25%, while low-conductivity silicone rubber robustly prevents the occurrence of an antenna effect.

SAR for realistic lead configurations

SAR simulation results for realistic lead configurations are presented in Fig. 5 and Table 2. In Fig. 5, 1 g local head SAR for all three electrode montages with center leads (see Fig. 3a–c) are shown. Adding electrodes, gel, and leads to Duke, changes the spatial variation of SAR, especially around the electrodes, but 1 g local head SAR is for all simulations in the same location as for the reference simulation. For 128 MHz simulations, 1 g local head SAR occurs on the skin on the left side of the neck while for 298 MHz it is in the cerebrospinal fluid. As seen in Table 2, only minimal changes to the B_1 field and SAR occur for 128 MHz and 298 MHz with circular electrodes, while the center-surround electrodes have more influence on the B_1 field, and therefore higher SAR after normalization.

Temperature measurements

One of the temperature measurements (indicated in Table 3) including the fitted model is shown in Fig. 6c. The modeled steady-state temperatures for all the measurements are listed in Table 3. Probe positions indicated in Table 3 are presented in Fig. 6a and b for the center-surround and circular electrodes, respectively.

For the circular electrodes at 3T, the highest temperature was observed on the posterior electrode for the anterior-posterior montage, with a temperature of 37.6 °C compared to 35 °C for the reference probe. For the right-left montage, the maximum temperature on the electrodes was only 1 °C higher than for the reference probe.

The center-surround electrodes at 3T showed the highest temperature increase (max 38.5 °C), with no observable difference between electrode pads with and without leads. Off-center leads also did not give rise to higher temperatures. For the pCASL sequence, the steady-state temperature was about 1 °C lower than for the RARE sequence in the same session, marked with an asterisk in Table 3.

Very limited increase was found for all measurements at 7T. The highest measured difference between the reference probe and a probe on the electrodes was 0.6 °C.

Stray field comparison

Fig. 7b and e show the fields from the leads calculated with Biot-Savart law using the tracked lead location seen in Fig. 7a and d. Fig. 7c and f are the measured current-induced fields in the MR scanner. The measured fields are both from currents flowing in the leads and in the subject's tissue. It is clear from comparing Fig. 7b and c that ΔB_{zc} is dominated by stray fields from the leads. With our optimized lead configuration with the silicone rubber leads as seen in Figs. 3a and 7d, where the leads are aligned in the z-direction, the stray field from the leads are greatly reduced (Fig. 7e) and therefore there is no relationship between lead stray field and ΔB_{zc} that is dominated by tissue currents.

Discussion

TES electrodes with copper leads pose a potential danger to the subject when used during an MRI session. Due to the coupling between the RF field of the scanner and the highly conductive leads, burns of the subject's scalp can occur unless appropriate measures are taken, such as adding safety resistors in a well-considered way. To minimize coupling between the RF field and the leads in general, we propose to use leads made with a low-conductivity material. By that, we gain flexibility to optimize the leads for the intended applications while ensuring safety. Additionally, this makes it easier to safely design more complex electrode configurations with multiple leads, such as the 4x1 montage [2] used for focal stimulation in TES-fMRI experiments. These electrodes and leads can relatively easily be constructed in-house from sheets of conductive silicone rubber.

In simulations, the antenna effect was found for odd multiples of ¼ RF wavelength (Fig. 4a), which is in agreement with previously reported experimental results [15] with the same boundary conditions. The antenna effect is often believed to occur at ½ RF wavelength only, but as pointed out by Balasubramanian et al. [15], this depends on the boundary condition of the leads. With low impedance at one end and high at the other, it occurs at ¼ RF wavelength, whereas with the same boundary condition at each end, e.g. immersed in tissue, antenna effect occurs at ½ RF wavelength.

Simulation results with varying lead conductivity at worst-case length (Fig. 4b) prove that the antenna effect will not occur for

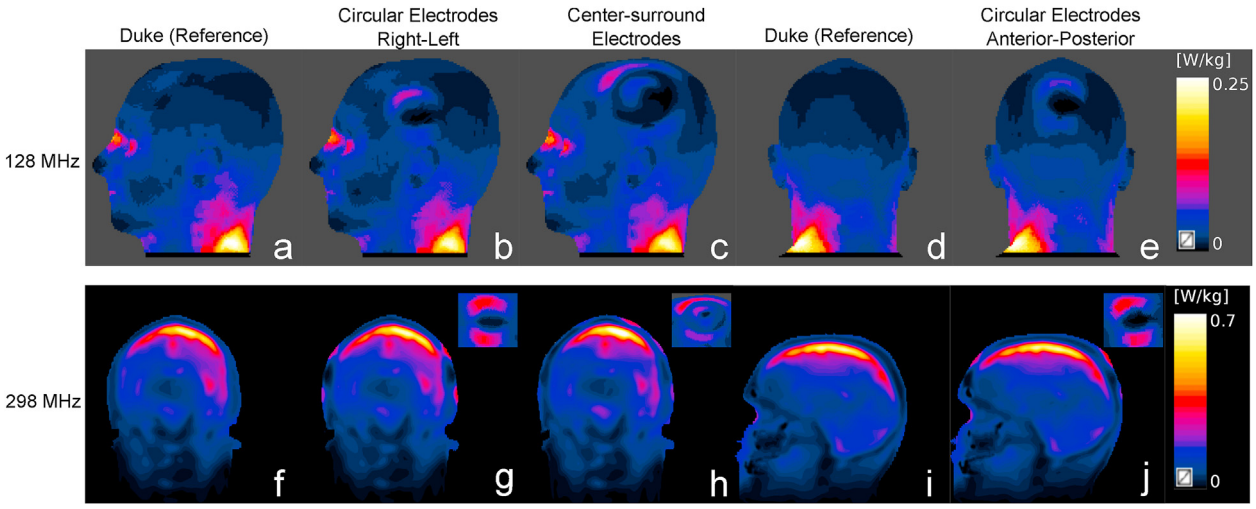

Fig. 5. 1 g average SAR for normalized B_1 for simulations at 128 MHz (top) and 298 MHz (bottom). Peak SAR for 128 MHz occurs on the skin of the left side of the neck, while it is in CSF for the 298 MHz simulations. A reference simulation of Duke without electrodes is shown in a), d), f), and i). The rest of the results are from simulations with electrodes and intended lead configurations (see Fig. 3a–c). Insets in the corner for g), h) and j) show the surface SAR around the electrodes.

silicone rubber with lead conductivity at 29.4 S/m. This increases the flexibility of the lead configuration and improves the experimental setup for MRCDI experiments. Additionally, no safety resistors are needed, which decreases the overall resistance of the leads compared to the conventional setup and allows for higher stimulation currents. This enables the use of increased stimulation current to study immediate and after-effects on BOLD activity using a standard stimulator. Also, safety resistors enforce nodes in electromagnetic waves, which may cause high local fields causing heating in nearby material and even resistor damage [24]. Careful design is needed to limit these effects and ensure appropriate distance from tissue. The simulations also show that carbon leads, which are often used as a safer alternative to copper leads, only reduce the severity of the antenna effect in our simulations by about 25%. Therefore, using carbon leads can provide a false sense of safety and has to be considered carefully for each specific case. Previous simulation work on a 256-electrode EEG cap has shown consistent results by comparing peak local SAR for varying lead conductivities [22]. The authors reported a 6-fold increase in peak 1 g local head SAR for high conductivities (including carbon) and no increase for conductivities below 100 S/m. The study was not for a specific resonance condition as in our case. Our results may therefore also be relevant for the EEG-MRI community.

Only very limited changes were observed for R_m and R_{1g} for all simulations with realistic lead configurations as seen in Table 2. In most cases the B_1 was slightly lower than $B_{1,ref}$ due to the additional load on the coil when electrodes and leads were included. For 1 W input power, this is also reflected in the slightly lower SAR for some simulations, especially with leads. For the same reason, all simulations with leads have lower SAR and more influence on B_1 than simulation without leads for 1 W input power. Slight changes to the spatial distribution of the RF field caused by electrodes and leads can also influence R_m and especially R_{1g}.

Overall, a very small change and mostly reduction in SAR is seen before B_1 normalization, while some increase in SAR is reported after normalizing. This is not seen as a problem since, if the scanner increases the input power, then the calculated SAR will be adjusted accordingly and the SAR safety limits will be reached earlier. In worst case, this will have an influence on the available ranges of sequence parameters, but not on safety.

Although the electrodes have an influence on local SAR values in the proximity to the electrodes as seen in Fig. 5, the 1 g local head SAR close to the electrodes does not exceed peak 1 g local head SAR already present in the reference simulation. The peak 1 g local head SAR was also in all simulations at the same location as for the reference simulations. Therefore, the local head SAR limits imposed by the scanner will still ensure conformance with the safety regulations. Additionally, in the 298 MHz simulations, the center-surround electrodes are located close to the locations of peak local head SAR without negative effect.

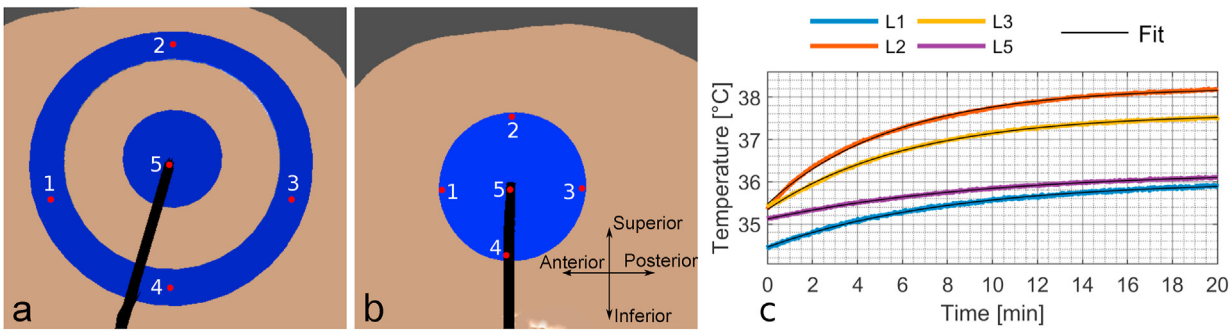

Fig. 6. In a) and b) the numbers on the electrodes indicate the probe position referred to in Fig. 6c and Table 3 c) Temperature measurement for center-surround electrodes with center leads (Fig. 3c). L in the legend indicates that it is a measurement on the left electrode. The black curves are the fitted models (Eqn (4)).

Table 2
Head SAR and local head SAR (1 g average) ratios (R_m and R_{1g}) for both field strengths and all simulated electrode montages compared to reference simulations. SAR is given for 1 W input power as well as normalized for the B_1 field in the center slice of the coil. The ratio between $B_{1,ref}$ and B_1 for the corresponding simulation is used for normalization. All local head SAR maxima were at the same location as for the reference simulation.

Frequency	Electrodes	Setup	Normalized to 1 W input			Normalized to B_1	
			R_m	R_{1g}	B_1^{ref}/B_1	R_m	R_{1g}
128 MHz	Circular Right-left	Without leads With leads	1.02 0.99	0.96 0.94	0.99 0.99	0.99 0.97	0.94 0.93
	Circular Anterior-posterior	Without leads With leads	1.02 0.96	1.00 0.93	0.99 1.02	1.00 1.01	0.98 0.98
	Center-surround	Without leads Center leads Off-center leads	1.01 0.97 0.94	0.94 0.86 0.91	1.01 1.02 1.06	1.02 1.01 1.04	0.95 0.90 1.01
298 MHz	Circular Right-left	Without leads With leads	1.00 0.98	1.00 1.00	1.01 1.02	1.03 1.02	1.02 1.04
	Circular Anterior-posterior	Without leads With leads	1.00 0.98	0.97 0.98	1.00 1.01	1.00 1.00	0.98 0.99
	Center-surround	Without leads Center leads Off-center leads	0.93 0.90 0.89	0.96 0.96 0.95	1.09 1.09 1.10	1.10 1.07 1.07	1.13 1.14 1.15

The highest measured temperature for the circular electrodes was on the posterior electrode. This is most likely not due to higher power dissipation on the electrode, but rather better thermal insulation as the head rests on the electrode and cushions.

At 3T, more heating was observed for the center-surround electrodes than the circular electrode. The heating was independent of lead position as well as whether leads were attached or not. In agreement with a previous study by Kozlov et al. [25], this indicates that the shape and size of the electrodes have high influence on heating. Therefore, care must be taken when designing new electrodes for TES-MRI experiments. The impedance around the ring of the center-surround electrode is about 300 Ω. Higher impedance would cause less heating, but it is a tradeoff between heating and homogeneous stimulation currents for focal stimulation. It has to be pointed out that the heating observed is with a high-SAR RARE sequence, which is not a recommended sequence for TES-MRI experiments. Usually, low-SAR echo planar imaging (EPI) or gradient-echo sequences will be used or in worst-case the pCASL sequence also tested in the temperature experiments. The pCASL sequence showed about 1 °C less heating than the RARE sequence. In contrast to our findings at 3T, a previous study reported much less heating on the center-surround electrodes [32]. The unspecified conductivity of the electrode material has high influence on the heating, but more importantly only an EPI sequence was used for the heat test. Since EPI used for fMRI experiments is usually a very low-SAR sequence at 3T, insignificant heating would be expected.

At 7T no considerable heating was observed. This is attributed to the fact that SAR is already higher at 7T for similar sequences, and the input power is therefore more restricted compared to 3T.

Although noticeable heating was measured on the center-surround electrodes at 3T, the temperatures were always lower than limits imposed by the international guidelines IEC 60601-2-33 [30] stating that the maximum tissue temperature has to be limited to 39 °C.

To further ensure safety and reduce the risk of resistor damage, the conventional electrodes and leads used in this work are limited to use with EPI sequences. The manufacturer requires removal of the cables when other sequences are used. Under the conditions evaluated, this is not necessary with low conductivity silicone rubber leads since no safety resistors are used and safety tests have been performed for high SAR sequences.

Table 3
Modeled steady state temperature from all measurements with various setups and probe positions. The numbers for the positions are indicated in Fig. 6a–b and L, R, A and P refer to electrode position (left, right, anterior and posterior). Ref is the reference probe on top of the head away from the electrodes. For the RARE sequence, the SAR was approximately 100% and for ASL, it was approximately 50%, varying slightly with subjects. The asterisks (*) indicate the same scan sessions for a RARE and pCASL sequence with electrodes and temperature probes in the same location. The double asterisks (**) indicate the data shown in Fig. 6c.

B_0	Electrodes	Setup	Sequence	Probe positions	Steady state temperature
3T	Circular	Right-left	RARE	[Ref L1 R3 L5]	[35.2 35.4 35.8 36.2]
		Anterior-posterior	RARE	[Ref A4 P2 P4]	[35.0 36.3 37.2 37.6]
	Center-surround	Without leads	RARE	[Ref L4 R2 L2]	[35.6 35.7 36.3 36.6]
				[L1 L5 L3 L2]	[35.9 36.4 37.2 38.4]
				[L1 L5 L3 L2]	[35.5 35.8 37.7 38.5]
		On-center leads	RARE	[Ref L4 L2 R2]	[35.6 36.2 37.2 37.2]
				[Ref L2 R2 L4]	[34.8 36.4 37.0 37.9]*
				[L1 L5 L3 L2]	[36.4 36.7 37.5 37.6]
				[L1 L5 L3 L2]	[36.0 36.2 37.6 38.2]**
		On-center leads	pCASL	[Ref L2 R2 L4]	[34.6 35.8 36.2 36.8]*
		Off-center leads	RARE	[Ref L4 L2 R2]	[35.4 36.2 37.0 37.3]
7T	Circular	Anterior-posterior	RARE	[A4 Ref P4 P2]	[34.9 35.3 35.7 35.9]
	Center-surround	On-center leads	RARE	[R2 L2 Ref L4]	[34.3 35.1 35.4 36.0]

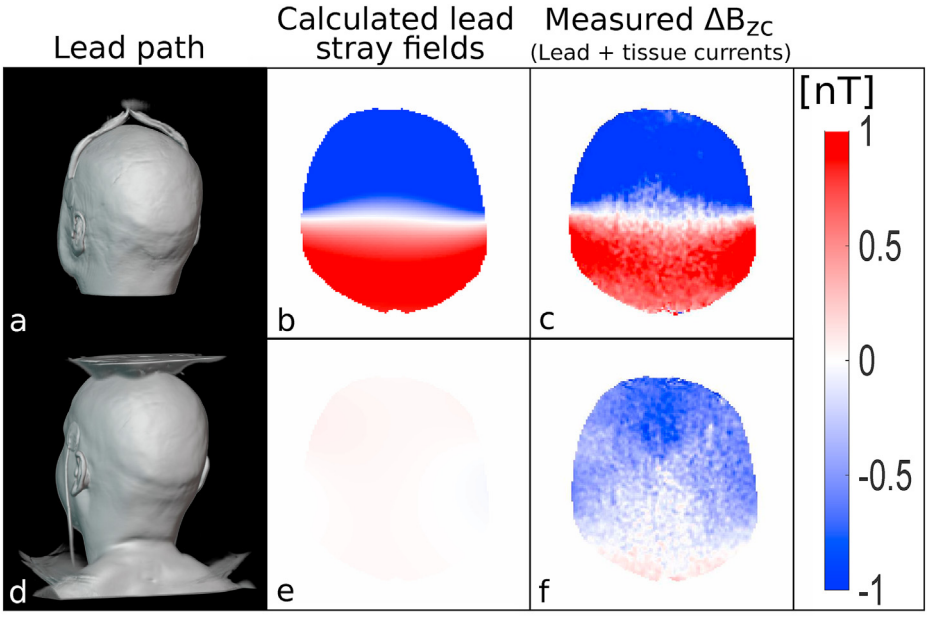

Fig. 7. a) and d) 3D ultra-short T_E images used to track the leads to calculate stray fields (See supplementary material S1). b) and e) are calculated stray fields from the two lead configurations. c) and f) are measured current-induced magnetic field changes. Image c) is clearly dominated by stray fields seen in image b), whereas the stray fields from leads in image e) are greatly reduced, so f) is dominated by tissue currents.

The rubber leads being visible on MR recordings without adding additional material is a practical benefit when doing stray field correction in MRCDI [9] (see supplementary material S1). Conventional copper leads and insulation are not visible on MRI, and therefore additional material needs to be attached around the leads before use. Attention must be paid to image distortions caused by chemical shift, gradient non-linearity, and concomitant fields, however.

The effect of the stray field on the measured ΔB_{zc} demonstrated in our MRCDI experiment necessitates correction by applying the Biot-Savart-Law [9,10]. However, any errors and inaccuracies of lead position estimation will have far less influence for the optimized cable configuration made possible by using silicone rubber leads. Additionally, the lead location cannot be tracked during ΔB_{zc} measurements. Therefore, any movements during the experiment will have detrimental effect on the stray field correction for the non-optimized setup.

The electrodes and leads have very limited and only superficial influence on B_1 and B_0 maps. However, when calculating the signal-to-fluctuation-noise ratio for an EPI time series, image artifacts having long ranging effects (centimeters) were found when copper leads and safety resistors were used. These artifacts were not found with silicone rubber leads. (see supplementary material S1).

Conclusion

We have proposed to use low-conductivity silicone rubber as leads for current injection electrodes in the MR scanner. This eliminates the potential safety hazard that comes with the coupling between high-conductivity materials and the RF field, such as the antenna effect that is not necessarily eliminated with carbon cables or safety resistors. For our setup, the simulations showed no increase in head SAR and head local SAR for both field strengths. Additionally, no temperature above the safety limits was recorded. Due to the increased flexibility of lead configurations, these electrodes offer an advantage for MRCDI experiments due to the reduction of compromising stray fields. For TES-MRI experiments, the maximum stimulation currents can be increased for voltage-limited stimulation devices due to lower overall resistance.

CRediT authorship contribution statement

Fróði Gregersen: Conceptualization, Methodology, Software, Validation, Formal analysis, Investigation, Writing – original draft, Visualization, Funding acquisition. **Cihan Göksu:** Software, Investigation, Writing – review & editing. **Gregor Schaefers:** Validation, Writing – review & editing, Supervision. **Rong Xue:** Resources, Writing – review & editing, Supervision, Funding acquisition. **Axel Thielscher:** Conceptualization, Methodology, Investigation, Writing – review & editing, Supervision, Funding acquisition. **Lars G. Hanson:** Conceptualization, Methodology, Investigation, Writing – review & editing, Supervision, Funding acquisition.

Declaration of competing interest

There are no known conflicts of interest associated with this publication and there has been no significant financial support for this work that could have influenced its outcome.

Acknowledgment

This study was supported by the Lundbeck Foundation (grants R313-2019-622 and R244-2017-196 to AT and R288-2018-236 to CG), the Chinese National Major Scientific Equipment R&D Project (grant ZDYZ2010-2) and a PhD stipend of the Sino-Danish Center for Education and Research to FG. The authors thank Zuo Zhentao, Hasan Hüseyin Eroğlu, Vincent Boer, and Esben Thade Petersen for kind technical help.

Appendix. A Supplementary data

Supplementary data related to this article can be found at https://doi.org/10.1016/j.brs.2021.02.019.

References

[1] Nitsche MA, Paulus W. Excitability changes induced in the human motor cortex by weak transcranial direct current stimulation. J Physiol 2000;527:633–9. https://doi.org/10.1111/j.1469-7793.2000.t01-1-00633.x.

[2] Datta A, Bansal V, Diaz J, Patel J, Reato D, Bikson M. Gyri-precise head model of transcranial direct current stimulation: improved spatial focality using a ring electrode versus conventional rectangular pad. Brain Stimul. 2009;2. https://doi.org/10.1016/j.brs.2009.03.005. 201–7, 207.e1.

[3] Opitz A, Paulus W, Will S, Antunes A, Thielscher A. Determinants of the electric field during transcranial direct current stimulation. Neuroimage 2015;109:140–50. https://doi.org/10.1016/J.NEUROIMAGE.2015.01.033.

[4] Saturnino GB, Thielscher A, Madsen KH, Knösche TR, Weise K. A principled approach to conductivity uncertainty analysis in electric field calculations. Neuroimage 2019;188:821–34. https://doi.org/10.1016/j.neuroimage.2018.12.053.

[5] Joy M, Scott G, Henkelman M. In vivo detection of applied currents by magnetic resonance imaging, vol. 7; 1989.

[6] Ider YZ, Birgül Ö. Use of the magnetic field generated by the internal distribution of injected currents for electrical impedance tomography (MR-EIT). Turk J Electr Eng Comput Sci 1998;6:215–26.

[7] Mosher JC, Leahy RM, Lewis PS. EEG and MEG : forward Solutions for inverse. Methods 1999;46:245–59.

[8] Fear EC, Hagness SC, Meaney PM, Okoniewski M, Stuchly MA. Enhancing breast tumor detection with near-field imaging. IEEE Microw Mag 2002;3:48–56. https://doi.org/10.1109/6668.990683.

[9] Göksu C, Scheffler K, Siebner HR, Thielscher A, Hanson LG. The stray magnetic fields in magnetic resonance current density imaging (MRCDI). Phys Med 2019;59:142–50. https://doi.org/10.1016/j.ejmp.2019.02.022.

[10] Göksu C, Hanson LG, Siebner HR, Ehses P, Scheffler K, Thielscher A. Human in-vivo brain magnetic resonance current density imaging (MRCDI). Neuroimage 2018;171:26–39. https://doi.org/10.1016/j.neuroimage.2017.12.075.

[11] Dempsey MF, Condon B. Review thermal injuries associated with MRI. Clin Radiol 2001;56:457–65. https://doi.org/10.1053/crad.2000.0688.

[12] Lemieux L. Recording of EEG during fMRI experiments: patient safety. MRM; 1997.

[13] Dempsey MF, Condon B, Hadley DM. Investigation of the factors responsible for burns during MRI. J Magn Reson Imag 2001;13:627–31. https://doi.org/10.1002/jmri.1088.

[14] Panych LP, Madore B. The physics of MRI safety. J Magn Reson Imag 2018;47:28–43. https://doi.org/10.1002/jmri.25761.

[15] Balasubramanian M, Wells WM, Ives JR, Britz P, Mulkern RV, Orbach DB. RF heating of gold cup and conductive plastic electrodes during simultaneous EEG and MRI. Neurodiagn J 2017;57:69–83. https://doi.org/10.1080/21646821.2017.1256722.

[16] Mosayebi Samani M, Agboada D, Jamil A, Kuo MF, Nitsche MA. Titrating the neuroplastic effects of cathodal transcranial direct current stimulation (tDCS) over the primary motor cortex. Cortex 2019;119:350–61. https://doi.org/10.1016/j.cortex.2019.04.016.

[17] Workman CD, Fietsam AC, Rudroff T. Different effects of 2 mA and 4 mA transcranial direct current stimulation on muscle activity and torque in a maximal isokinetic fatigue task. Front Hum Neurosci 2020;14:1–11. https://doi.org/10.3389/fnhum.2020.00240.

[18] Chhatbar PY, Chen R, Deardorff R, Dellenbach B, Kautz SA, George MS, et al. Safety and tolerability of transcranial direct current stimulation to stroke patients – A phase I current escalation study. Brain Stimul. 2017;10:553–9. https://doi.org/10.1016/j.brs.2017.02.007.

[19] Workman CD, Fietsam AC, Uc EY, Rudroff T. Cerebellar transcranial direct current stimulation in people with Parkinson's disease: a pilot study. Brain Sci 2020;10. https://doi.org/10.3390/brainsci10020096.

[20] Nitsche MA, Bikson M. Extending the parameter range for tDCS: safety and tolerability of 4 mA stimulation. Brain Stimul. 2017;10:541–2. https://doi.org/10.1016/j.brs.2017.03.002.

[21] Angelone LM, Vasios CE, Wiggins G, Purdon PL, Bonmassar G. On the effect of resistive EEG electrodes and leads during 7 T MRI: simulation and temperature measurement studies. Magn Reson Imaging 2006;24:801–12. https://doi.org/10.1016/j.mri.2006.01.006.

[22] Atefi SR, Serano P, Poulsen C, Angelone LM, Bonmassar G. Numerical and experimental analysis of radiofrequency-induced heating versus lead conductivity during EEG-MRI at 3 T. IEEE Trans Electromagn C 2019;61:852–9. https://doi.org/10.1109/TEMC.2018.2840050.

[23] Jorge J, Grouiller F, Ipek Ö, Stoermer R, Michel CM, Figueiredo P, et al. Simultaneous EEG-fMRI at ultra-high field: artifact prevention and safety assessment. Neuroimage 2015. https://doi.org/10.1016/j.neuroimage.2014.10.055.

[24] Kozlov M, Müller R, Pampel A, Kalloch B, Weiskopf N, Möller HE. RF safety of transcranial direct current stimulation equipment during MRI. 2018. Poster Present Jt Annu Meet ISMRM-ESMRMB 2018, Paris, Fr.

[25] Kozlov M, Horner M, Kainz W, Weiskopf N, Möller HE. Modeling radiofrequency energy-induced heating due to the presence of transcranial electric stimulation setup at 3T. Magn Reson Mater Phys Biol Med 2020. https://doi.org/10.1007/s10334-020-00853-5.

[26] Datta A, Elwassif M, Battaglia F, Bikson M. Transcranial current stimulation focality using disc and ring electrode configurations: FEM analysis. J Neural Eng 2008;5:163–74. https://doi.org/10.1088/1741-2560/5/2/007.

[27] Gosselin MC, Neufeld E, Moser H, Huber E, Farcito S, Gerber L, et al. Development of a new generation of high-resolution anatomical models for medical device evaluation: the Virtual Population 3.0. Phys Med Biol 2014;59:5287–303. https://doi.org/10.1088/0031-9155/59/18/5287.

[28] Wolf S, Diehl D, Gebhardt M, Mallow J, Speck O. SAR simulations for high-field MRI: how much detail, effort, and accuracy is needed? Magn Reson Med 2013;69:1157–68. https://doi.org/10.1002/mrm.24329.

[29] van Lier ALHMW, Kotte ANTJ, Raaymakers BW, Lagendijk JJW, van den Berg CAT. Radiofrequency heating induced by 7T head MRI: thermal assessment using discrete vasculature or pennes' bioheat equation. J Magn Reson Imag 2012;35:795–803. https://doi.org/10.1002/jmri.22878.

[30] IEC. Particular requirements for the basic safety and essential performance of magnetic resonance equipment for medical diagnosis. 2010. IEC 60601-2-33.

[31] Barbalace K. Periodic table of elements: sorted by electrical conductivity. EnvironmentalChemistry.com; 1995. https://environmentalchemistry.com/yogi/periodic/electrical.html. accessed October 14, 2019.

[32] Gbadeyan O, Steinhauser M, Mcmahon K, Meinzer M. Safety, tolerability, blinding efficacy and behavioural effects of a novel MRI-compatible, high-definition tDCS set-up. Brain Stimul. 2016. https://doi.org/10.1016/j.brs.2016.03.018.